Wen Wu, Jung-Hee Seo, Charles Meneveau, and Rajat Mittal. "Response of a Laminar Separation Bubble to Zero-Net Mass Flux Actuation", 2018 Flow Control Conference, AIAA AVIATION Forum, (AIAA 2018-4018) https://doi.org/10.2514/6.2018-4018

Response of a Laminar Separation Bubble to Forcing with Zero-Net Mass Flux Jets

Wen Wu*, Jung-Hee Seo†, Charles Meneveau‡, and Rajat Mittal§
Mechanical Engineering, Johns Hopkins University, Baltimore, MD, 21218

The response of a laminar separation bubble to forcing by zero-net mass flux (ZNMF) jets is investigated via direct numerical simulations. The Reynolds number based on the inflow boundary layer thickness and the freestream velocity is 1,000 and a suction-blowing velocity distribution imposed at the top boundary of the computation domain is used to create a closed separation bubble. The ZNMF actuators are placed upstream of the separation point and three different actuator jet configurations are considered, including two-dimensional and rectangular jet slots. For all cases, the reverse-flow region is significantly reduced by the forcing but the boundary-layer displacement effect remains significant. The three-dimensionality of the turbulent structures depends on the spanwise scale of the actuator, while short-wavelength unsteadiness persists among the cases downstream of the reattachment point. The total mechanical energy is consumed by either viscous or turbulent effects, and can be visualized and analyzed using energy transport analysis.

I. Introduction

Zero-net mass flux (ZNMF) devices have been shown to be effective for control of flow separation and associated drag reduction and lift augmentation control surfaces ([1–11], among others). The successful control of boundary-layer separation using ZNMF actuators is determined by a multitude of parameters. Among others, two key operational parameters are: the ratio of the actuator velocity to the freestream velocity, V_{jet}/U_∞ (or alternatively the oscillatory blowing momentum coefficient, $C_\mu = \rho V_{\text{jet}}^2 d/(q_\infty c)$ where d is the jet width and c the chord length)[3–5]; and the dimensionless frequency of the jet, $F_{\text{jet}}^+ = f_{\text{jet}}/f_n$, where f_n is a frequency associated with some intrinsic time scale in the undisturbed flow[6, 7]. Several studies have shown that efficient control is achieved for forcing frequencies near the frequency of the separation bubble instability regardless of the form of actuation[8–11].

Despite significant work on this topic, many fundamental questions regarding the response of the separation bubble to ZNMF forcing have not been answered. In particular the effect of actuator frequency, duty cycle, amplitude as well as the actuator slot geometry are not well characterized and formulation of universal principles that could help predict the performance of these actuators is missing. In this study, we will focus on a laminar boundary layer with a separation induced by an adverse pressure gradient (APG). Unsteady perturbations mimicking the ZNMF actuator will be applied to modulate the boundary layer upstream of the flow separation. A particular focus of the current research is the effect of the actuator slot configuration on the control authority and the flow physics associated with the interaction of these three-dimensional perturbations with the separation bubble. In the following, we first briefly describe the numerical methodology, and then discuss the mean flow development, as well as the turbulent features and structures; and finally describe the response of the separation bubble from the view point of energy and dissipation.

II. Methodology

Incompressible Navier-Stokes equations are solved using a well-validated, in-house finite difference code ViCar3D[12]. The spatial derivatives are computed using a second-order accurate, central-difference scheme. A

*Postdoctoral Fellow and AIAA Member.
†Associate Research Professor and AIAA Member
‡Professor and AIAA Senior Member
§Professor and AIAA Associate Fellow

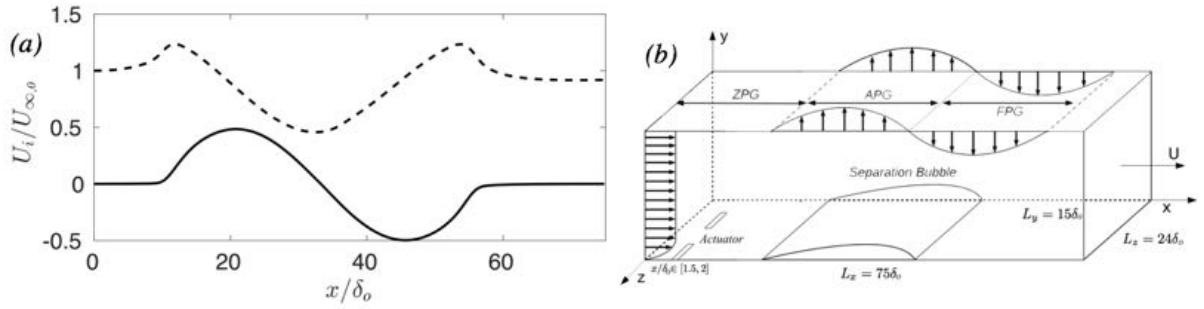

Fig. 1 *(a)* Imposed suction-blowing velocity distribution along the top boundary. Solid line, V_{top}; dashed line, U_{top} obtained by zero vorticity condition; *(b)* Schematic of computational domain (not to scale).

second-order Adams-Bashforth scheme is employed for the convective terms, while the diffusion terms are discretized using an implicit Crank-Nicolson scheme that eliminates the viscous stability constraint. The equations are integrated in time using a two-stage fractional step method. The Poisson equation for the pressure is the most CPU intensive step of the time-integration and ViCar3D employs a suite of sparse matrix solvers including geometric multigrid and preconditioned conjugate gradient (BiCGSTAB) for efficient solution of the equation on multi-processors. The code is fully parallelized using MPI; the code scales well on up to 1000+ processors and has been ported to a wide variety of platforms.

The calculation domain is shown in Fig. 1 *(b)*. The scales used for normalization are the freestream velocity at the ($U_{\infty,o}$) and boundary layer thickness (δ_o, where the flow velocity has essentially reached $0.99U_{\infty,o}$) of the Blasius velocity profile at the assigned inlet of the calculation domain (denoted by subscript $(.)_o$). The Reynolds number of the flow is $Re = U_{\infty,o}\delta_o/\nu = 1000$. The domain spans $75\delta_o$ in the streamwise direction, $15\delta_o$ in the wall-normal direction and $24\delta_o$ in the spanwise direction. The sufficiency of this spanwise domain size is assessed by two-point correlation of the spanwise stochastic fluctuation. Blasius velocity profiles are assigned at the inlet, while a convective boundary condition is used for the outlet. A no-slip condition is used on the bottom surface. Periodic boundary conditions are applied in the spanwise direction.

At the top boundary, a suction-blowing boundary condition is used to generate a finite size separation bubble (Fig. 1 *(a)*). The profile of the wall-normal velocity reads

$$V_{\text{top}}(x) = -V_s \sin\left(\frac{2\pi(x - x_s)}{L_s}\right) \exp\left(-a_s \left(\frac{2(x - x_s)}{L_s}\right)^b\right) \tag{1}$$

where $V_s = 0.5U_{\infty,o}$, $x_s = 33\delta_o$, $L_s = 50\delta_o$, $a_s = 10$, and $b_s = 20$. This configuration has been widely used in the research on APG effects because it avoids the streamline curvature effects (see [13–16] among others). The streamwise velocity satisfies zero mean-spanwise-vorticity condition at the top boundary. The same profile has been used in recent studies by the present authors on the effect of actuator modulation schemes on the reduction of a laminar separation bubble[17].

The actuators used are synthetic (or ZNMF) jets from spanwise slots located between $x = 1.5$ and 2. Results reported here employed an array of spanwise arranged jets with the same sinusoidal jet velocity waveform and phase given by $V_{\text{jet}} = A_f \sin(2\pi f t)$ (where $A_f = 0.2U_{\infty,o}$ is the magnitude). The frequency used in this study is $f = 0.06\delta_o/U_{\infty,o}$, which matches the observed natural frequency of the bubble in the undisturbed case; thus, $F^+_{\text{jet}} = 1$. The streamwise velocity at the outlet of the synthetic jet is set to zero when V_{jet} is positive and Neumann condition with zero gradient, however, is imposed during the ingestion phase to ensure a more realistic velocity distribution near the jet exit.

Actuators of three different sizes in the spanwise (denoted as d) are tested in this study. The parameters of their configurations are listed in Table 2. The ratio of the ZNMF jet momentum flux to the base flow momentum flux

$$C_\mu = \frac{V^2_{\text{jet,RMS}} d}{U^2_{\infty,o} L_z}, \tag{2}$$

where $V_{\text{jet,RMS}}$ is the root-mean-squared value of the ZNMF jet velocity, varies between the cases due to the difference in d. Grid-converged results are achieved by using 688×128×192 grids in the three directions respectively. The grid is uniform in the spanwise direction and stretched near the wall normal direction. In the streamwise direction the grid is refined near the location of the actuator to resolve the actuator by 12 points in the streamwise direction.

Table 1 Simulation parameters of the actuator

Parameters/Cases	d, jet width in z	jet spacing in z	jet range in x	C_μ
No jet	-	-	-	-
2D jet	$24\delta_o$	-	$[1.5\delta_o, 2\delta_o]$	0.02
3D jet6	$6\delta_o$	$6\delta_o$	$[1.5\delta_o, 2\delta_o]$	0.01
3D jet3	$3\delta_o$	$3\delta_o$	$[1.5\delta_o, 2\delta_o]$	0.01

Table 2 Simulation parameters of the actuator

Parameters/Cases	d, jet width in z	jet spacing in z	C_μ
No jet	-	-	-
2D jet	$24\delta_o$	-	0.02
3D jet6	$6\delta_o$	$6\delta_o$	0.01
3D jet3	$3\delta_o$	$3\delta_o$	0.01

III. Results and discussion

A. Turbulent structures

The vortex structures for the various cases are shown in Fig. 2. In the undisturbed case, the separating boundary layer is still smooth and laminar on the front side of the separation bubble and no turbulent structures are observed in that region (Fig. 2 *(a)*). On the downstream side of the bubble, two-dimensional vortex rollers are generated (see $x \approx 40$) by the Kelvin–Helmholtz instability. The shedding frequency, namely the natural frequency of the separation bubble, is estimated to be $0.06\delta_o/U_{\infty,o}$. These roller vortices get distorted by a secondary instability as they convect towards the reattachment point at $x = 52$ and become three-dimensional in the reattached flow.

Compared with the undisturbed case, the vortices observed in the three forced cases are more complex. There are bundles of vortices travelling near the bottom surface throughout the streamwise direction. No obvious detachment from the wall, nor vortex roller generation far away in the main stream is observed. As we will discuss in the next subsection, the separation bubble is significantly decreased by the forcing. When 2D forcing is applied, the slot actuator creates strong two-dimensional spanwise roller vortices (*e.g.* near $x = 2$, 8 and 13 at the time instant showed in Fig. 2 *(b)*). Around $x = 20$ the secondary instability forms peak-and-valley waveform along the spanwise direction in these rollers. There are also streamwise braid vortices formed between two consecutive rollers between $x = 20$ and 27. The 2D vortex roller rapidly breaks up and becomes three dimensional as it moves further downstream.

The 3D forcing jets introduce spanwise perturbations to the laminar boundary layer. As can be seen from Fig. 2 *(c,d)*, these actuators generate much shorter vortices in z during forcing. The spanwise shear formed by the jets and the undisturbed part in between also induces vortex structures which are elongated by the mean wall-normal velocity gradient and form inclined 'legs' of the short vortex roller (for instance, see region $x = 5$ to 10 in Fig. 2 *(c,d)*). Downstream of the expected separation point ($x = 7$ in the undisturbed case), bundles of hairpin vortices are formed. As these eddies travel further downstream, they form large-scale structures non-uniformly distributed in the spanwise direction. The locations of these large-scale structures appear be correlated to the position of the actuators upstream.

The presence of these eddies amplifies the interaction between the laminar boundary layer and the freestream. Such interaction is a key factor for separation control: bringing high-momentum fluid towards the wall decreases the near-wall momentum deficit caused by the APG and this delays the flow separation and reduce the size of the separation bubble. Figure 3 shows the turbulent kinetic energy (TKE) to demonstrate the intensity of velocity fluctuations in these flows. The boundary layer edge (solid line) and mean $U = 0$ (dashed line) are superposed, which shows that the separation bubble is indeed reduced by the forcing. We will discuss this in more detail in the next section. Without forcing, only weak TKE is observed near the reattachment point. When forcing is applied, large TKE appears around $x = 20$ where the flow experiences APG, indicating strong interaction between the vortices when the mean flow slows down. The

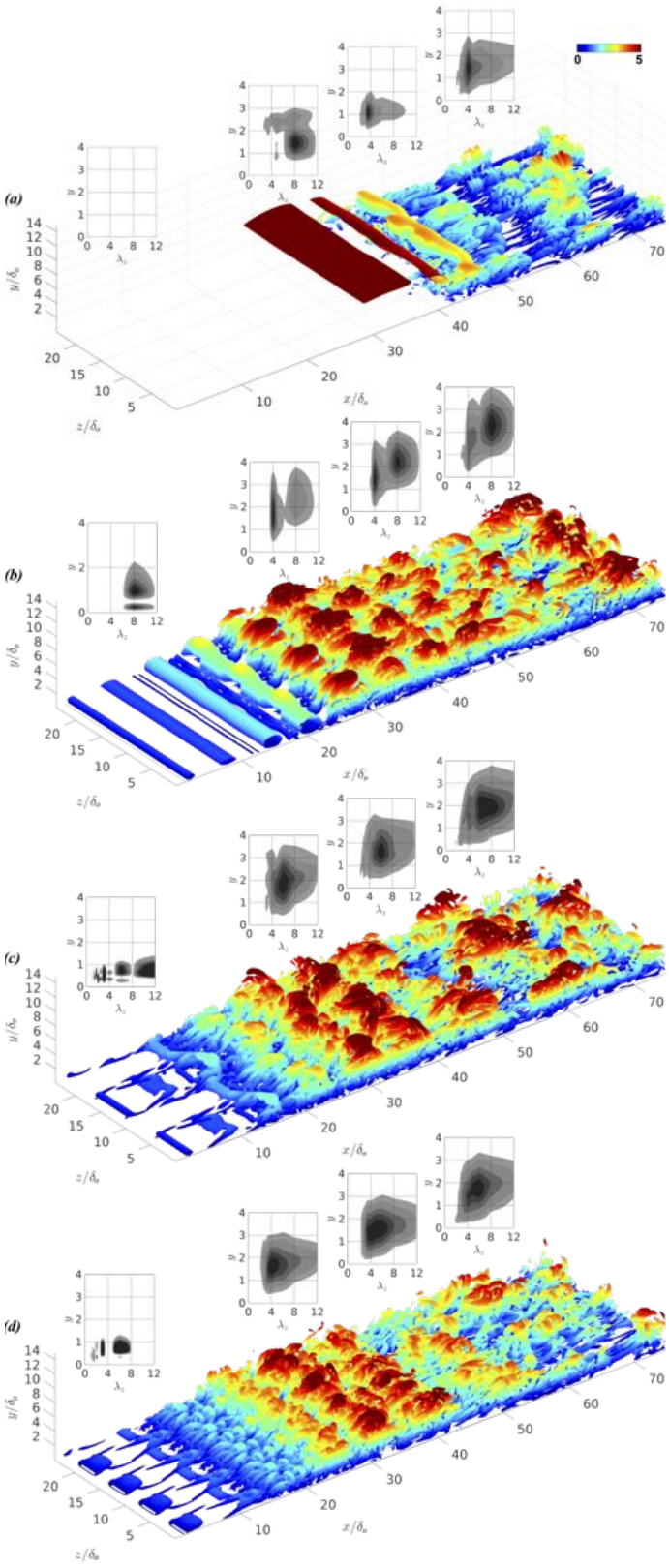

Fig. 2 Instantaneous flow structures shown by isosurfaces of the second invariant of the velocity gradient tensor $Q = 0.015U_{\infty,o}^2/\delta_o^2$, colored by distance from the bottom wall. *(a)* no jet, *(b)* 2D jet, *(c)* 3D jet6 and *(d)* 3D jet3. Inset shows the pre-multiplied spanwise spectrum of the fluctuating u-velocity at $x = 10$, 45, 55 and 65. For the undisturbed case no spectrum is obtained at $x = 10$.

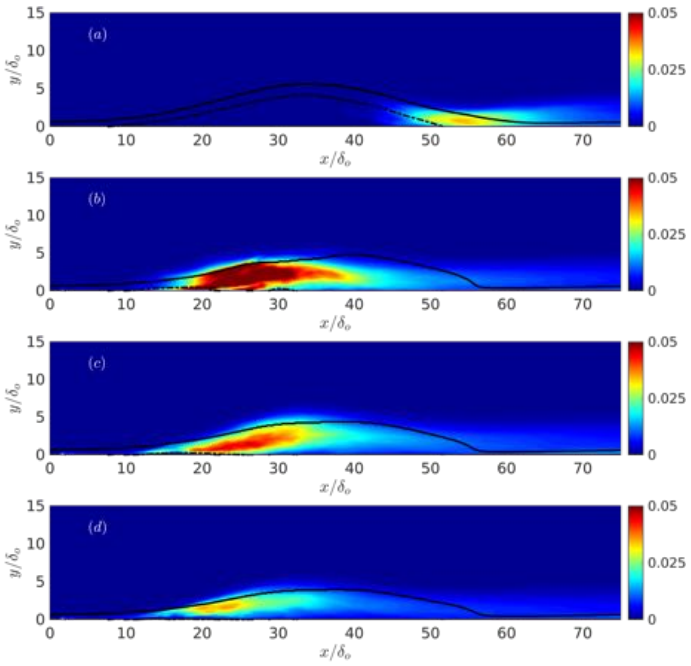

Fig. 3 Contours of turbulent kinetic energy. Solid line, boundary layer edge, *i.e.*, $U = 0.99U_\infty$; dashed line $U = 0$. *(a)* no jet, *(b)* 2D jet, *(c)* 3D jet6 and *(d)* 3D jet3.

peak TKE seems to be negatively correlated with the size of the jet, an effect that can be due to two reasons: either the longer jet adds more disturbance to the flow (because C_μ is higher), or the interaction between the spanwise-coherent structures is more intense.

The spanwise scale of the turbulent structures can be quantitively measured by the pre-multiplied energy spectrum of the fluctuating velocity. To obtain the spectra, the two-dimensional two-point autocorrelation coefficient in the spanwise direction is firstly calculated by

$$R_{ij}(x, y, r_z) = \frac{\overline{u_i'(x, y, z)u_j'(x, y, z + r_z)}}{\overline{u_i'(x, y, z)u_j'(x, y, z)}} \tag{3}$$

where r_z is the displacement between two points in z. Average (denoted as $\overline{(.)}$) is taken in the spanwise direction and in time. A Fourier transformation in the spanwise direction of the computed correlation yields the energy spectrum of velocity fluctuations as a function of the spanwise wavenumber (k_z)

$$\phi_{ij}(x, y, k_z) = \frac{1}{2\pi} \int_{-\infty}^{\infty} R_{ij}(x, y, r_z) \mathrm{e}^{-ik_z r_z} dr_z \tag{4}$$

For the undisturbed case, the natural shedding generates two-dimensional eddies around $x = 30$ (refer to Fig. 2 *(a)*). The inset of Fig. 2 *(a)* shows that the spanwise length scale (expressed in terms of wavelength $\lambda_z = 2\pi/k_z$) of these eddies is $\lambda_z = 8\delta_o$ at $x = 45$, indicting the formation of peak-valley shape due to the secondary instability. The wall-normal position of the structures at this x-location is about y=1.5. Downstream at $x = 55$, this length scale decreases to $\lambda_z = 4\delta_o$ and its variation further downstream is small. The energy at the same level is distributed over a larger area in the diagram, indicating the eddies grow in the vertical direction between $x = 55$ and 65.

Disturbed by the 2D actuators, strongly coherent spanwise rollers are generated at $x = 2$. Three dimensionality develops rapidly: by $x = 10$ the dominant wavelength of the structures is $8\delta_o$ (refer to inset of Fig. 2 *(b)*). The footprint of this scale persists throughout the domain while smaller scale eddies with $\lambda_z = 4\delta_o$ develop downstream. This short wavelength represents the three-dimensionality of the flow after reattachment and it coincides with one in the undisturbed case. Similarly, when the actuator width is $3\delta_o$ (*i.e.*, disturbance wavelength being $\lambda_z = 6\delta_o$), the dominant wavelength at $x = 10$ is $6\delta_o$ (refer to inset of Fig. 2 *(c)*) and this peak still contains a significant amount of energy at $x = 65$. The wavelength $4\delta_o$ shows up as an inherent scale due to the non-linear interaction between the instabilities. When the actuator width is $6\delta_o$, the wavelength of the forcing is $12\delta_o$ at $x = 10$ as expected (refer to inset of Fig. 2 *(d)*)

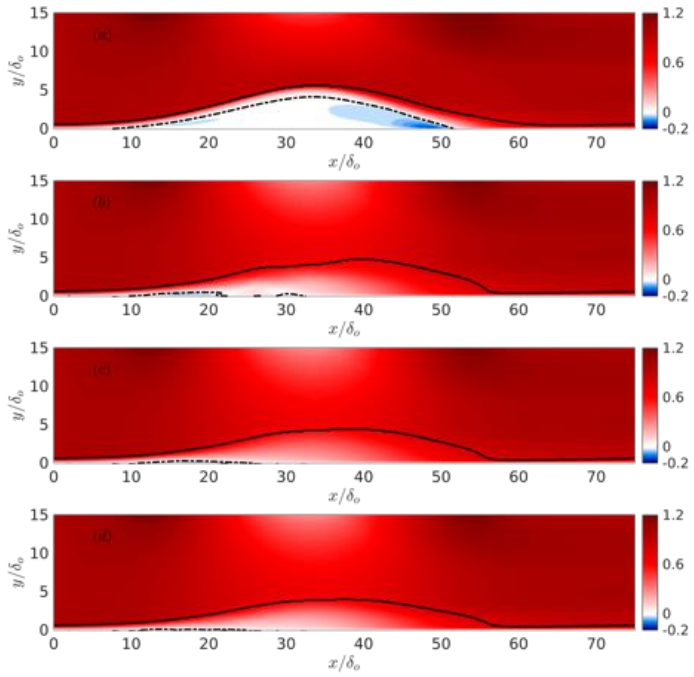

Fig. 4 Contours of the mean velocity. Solid line, boundary layer edge, *i.e.*, $U = 0.99U_{\infty,o}$; dashed line $U = 0$. Cases: *(a)* no jet, *(b)* 2D jet, *(c)* 3D jet6 and *(d)* 3D jet3.

but only its subharmonic scale at $\lambda_z = 6\delta_o$ appears at further downstream locations. It may be caused by the long wavelength that exceeds the one naturally generated in the undisturbed or 2D forcing case (*i.e.*, $\lambda_z = 8\delta_o$). Note that the inherent wavelength $4\delta_o$, again, already appears at $x = 45$ and persists at other downstream locations.

B. Mean flow characteristics

The separation region can be described by the backflow region in the mean velocity field, or on the wall by the region of negative $C_f = \tau_w/(1/2U^2_{\infty,o})$ (subscript $(.)_w$ denotes quantities at the wall). Significant reduction in the separation area for the cases with actuation can be confirmed by looking at Fig. 4 and Fig. 5. Without the actuator (Fig. 4 *(a)*), the separation bubble is about $45\delta_o$ long on the wall and its maximum thickness is $4\delta_o$. When the forcing is applied, the mean reverse flow region (solid lines showing $U = 0$ in Fig. 4) shrinks to a very thin layer between $x = 10$ to 30 regardless of the spanwise length of the actuators. The decrease of separation area on the wall can also be identified by the profile of C_f shown in Fig. 5, in which the region where C_f is negative becomes much smaller with the forcing and only small magnitudes of negative C_f are observed. The strong backflow region near the reattachment point in the undisturbed case (around $x = 49$) disappears. The actuator clearly affects the moment and energy transfer between the main stream and the boundary layer and prevents the occurrence of massive backflow.

The profile of $C_p = (p_w - p_{w,o})/(1/2\rho U^2_{\infty,o})$ is compared (Fig. 4 *(b)*) where the inviscid pressure distribution is plotted for comparison. Without forcing, the C_p profile shows a plateau inside the separation bubble. A peak of pressure is formed at the reattachment point due to the stagnation of impinging flow and the general shape of the C_p profile deviates significantly from the inviscid profile. These are traditional signatures of massive flow separation. Conversely, with the forcing by the actuator the flow in the low velocity region is almost horizontal thus the stagnation pressure peak does not appear and the overall trend of the profile agrees with the inviscid pressure distribution. The remaining difference is due to the viscous effects within the laminar boundary layer in the vicinity of the wall.

The C_f and C_p profiles compared between the three forced cases are quite similar. Slight differences can be seen in the APG region ($x \leq 33$): the mild negative C_f region near $x = 18$ vanishes as the actuators become more three-dimensional in the spanwise direction; correspondingly, the C_p profile at the same location shows a continuous increase without the appearance of inflection point as in the other two forced cases. This is due to the more rapid breakup of the spanwise roller vortices due to 3D forcing detailed in the previous section. It is however noted that there is still a large area in the flow where the velocity deficit is significant: in fact, the position of the boundary layer edge

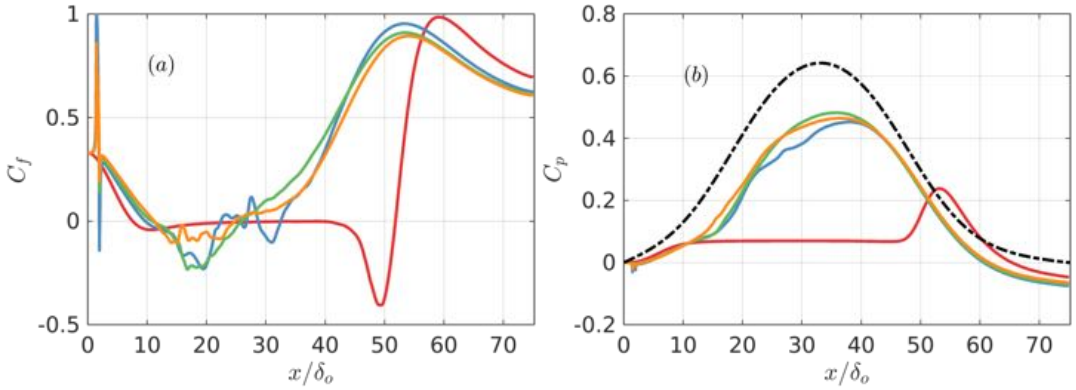

Fig. 5 Profiles of *(a)* C_f and *(b)* C_P. — · — in *(b)* the symmetric inviscid wall-pressure distribution. Cases: no jet; 2D jet; 3D jet6; 3D jet3.

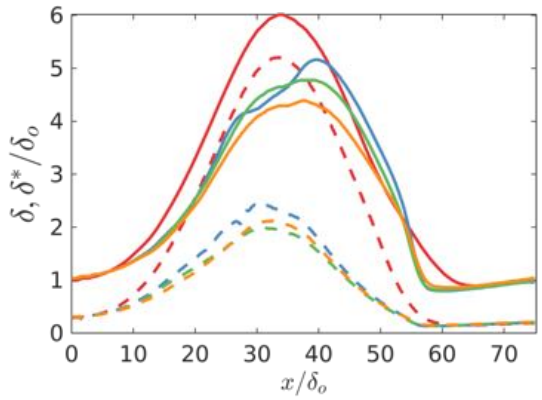

Fig. 6 Profiles of the boundary layer thickness δ (solid lines) and displacement thickness δ^* (dashed lines). Line colors same as used in Fig. 5.

changes slightly between cases (solid lines in Fig. 6). The maximum displacement thickness (dashed lines in Fig. 6) is reduced by 50 to 60 percent by the forcing but not as significantly as the reduction of reverse flow region.

C. Analysis of the energy transport and transport line visualization

An important consideration when designing diffusers is the loss of mechanical energy due to flow separation. The introduction of a actuator for separation control might diminish separation but at the same time, enhance turbulent diffusion and has the potential to cause additional total energy loss. In this section we will estimate the energy loss quantitively, visualize its transport using a recently proposed flow visualization tool, and discuss the effects of ZNMF forcing on the energy budget.

Recently, Meyers and Meneveau [18] developed a technique to visualize and analyze the transport of momentum and total energy in turbulent shear flow. They generalized the notion of streamline and streamtubes (based on mass flux or volume flux) and proposed transport lines and tubes appropriate to visualize the transport of mean momentum and total energy. Such transport tubes have the property that no fluxes of the momentum or energy occur over their respective tube mantles while transport lines are tangential to the total flux of the respective quantities. The approach is similar to the heat lines sometimes used in convective heat transfer[19]. We use this methodology to analyze the transport of total energy and contrast it to the transport of mass (streamlines), and we provide integral measures of the total energy flux to compare cases with and without forcing.

The approach is based on the transport equation for the total mechanical energy in the mean flow, defined as

$$E = U_i U_i/2 + P/\rho, \tag{5}$$

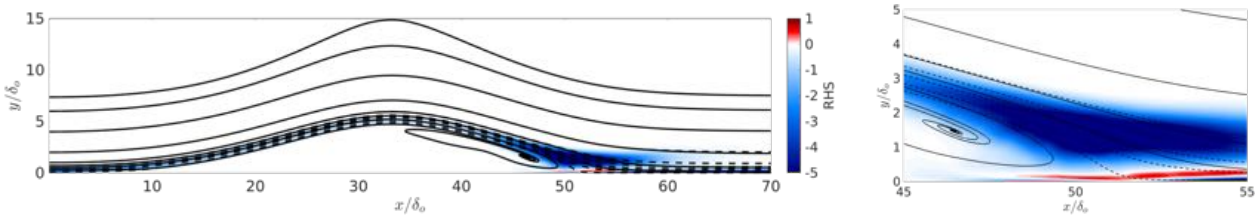

Fig. 7 Transport lines of E, total mechanical energy in the mean flow (solid lines) and classical streamlines of the mean flow (dashed lines), for the case without actuation. The color contours show the RHS of Eq. (6), including the negative of TKE production and viscous dissipation of mean mechanical energy. Right figure shows a zoom near the reattachment point.

After Reynolds averaging the equations, the transport equation of E can be written as follows:

$$\frac{\partial}{\partial x_k}\left(EU_k + U_i\overline{u_i'u_k'} - 2\nu S_{ik}U_i\right) = \overline{u_i'u_k'}\frac{\partial U_i}{\partial x_k} - 2\nu S_{ik}\frac{\partial U_i}{\partial x_k}, \tag{6}$$

where it is apparent that the following vector field

$$F_{E,k} = EU_k + U_i\overline{u_i'u_k'} - 2\nu S_{ik}U_i \tag{7}$$

is the total flux vector field of E including advection by the mean velocity and surface done by the Reynolds and viscous stresses. The transporting velocity field can be defined according to

$$U_{E,k} = \frac{F_{E,k}}{E} = U_k + \frac{U_i\overline{u_i'u_k'} - 2\nu S_{ik}U_i}{E}. \tag{8}$$

Therefore, an energy transport tube (or transport line for the two-dimensional time and spanwise averaged flow field) coincide with the streamtube (or streamline) when both the Reynolds stresses and viscosity are zero. Selected energy lines for the undisturbed case are shown in Fig. 7. Streamlines originating from the same positions are also plotted. It can be seen that the energy lines deviate significantly from the streamlines near the wall and in the separation region. The last energy line shown in the figure starts from the inflow at $y = 7.36$ and all the energy brought by the fluid entering the domain below this position stays inside the calculation domain. Note that Eq. (6) is in the form of $\nabla \cdot \phi = \text{RHS}$, while the RHS is not zero. So the energy is non-conservative during the transport and the Reynolds and viscous stresses act (typically) as sinks of E (note that the turbulence TKE production term could be positive, however). The color contours shown in the background of Fig. 7 are mostly negative (sink of energy). We have checked that the viscous term is the only sink in the separating shear layer, until vortex shedding occurs and turbulence becomes dominant. In particular, near the reattachment point, the RHS in fact has some positive values near the wall, indicating that the energy is transferred from the fluctuating turbulence to the mean flow (backscatter). Also notable is the appearance of a spiral attracting node inside the separated region.

To evaluate the energy loss, we calculate the total energy flux at each streamwise location between the wall and a particular energy line starting at $x = 0$, $y = 3$. The streamwise behavior of total energy flux below the chosen energy transport line are plotted in Fig. 8. The case of Blasius laminar boundary layer is included for reference which only contains the laminar advection and viscous flux based on the Blasius solution. The decreasing trend implies that as the flow proceeds downstream, it loses energy. Ultimately sufficiently downstream the entire inflow energy is lost when the energy transport line turns and ends at the wall, and this is similar to the case of Couette flow considered earlier [18]. The undisturbed case agrees with the Blasius solution very well up to x=45 and this indicates that despite the boundary layer having separated, the energy dissipation by the viscous term in Eq. (6) stays essentially the same as the one in the attached Blasius boundary layer. Because there is no shedding, the Reynolds stresses and the turbulent diffusion contribution is zero. As the vortex shedding starts near the reattachment point, energy loss become more severe.

Results also show that when the actuators are used, the energy loss deviates from the Blasius flow much earlier, from x=10, and more energy is lost in total by the end of the calculation domain, due to enhanced turbulent diffusion. Comparing the three forced cases, the 2D and wide 3D jets produce similar amount of energy loss, while the narrow actuators shows intermediate loss. Therefore, it seems that more three-dimensional actuators reduce the separation bubble with a lower net energy loss than 2D ZNMF jets.

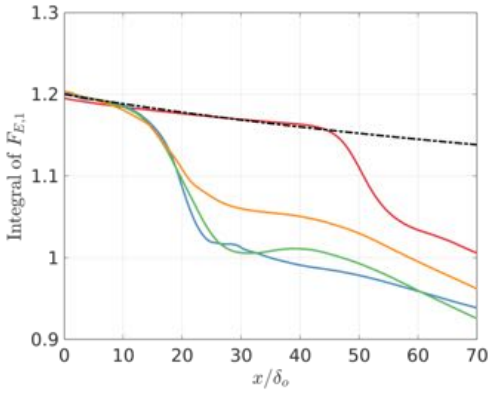

Fig. 8 Integral of total energy flux (refer to Eq. (6)) between the wall and the energy line originating from $x/\delta_o = 0$, $y/\delta_o = 3$. Line colors same as Fig. 6. Dash-dot line being the one obtained by Blasius boundary layer.

IV. Conclusions

Using DNS, we studied unsteady laminar separation and its response to ZNMF jets with different spanwise length scales. The actuators significantly reduce the mean backflow region by enhancing the turbulent interaction between the near-wall flow and the freestream. The finite spanwise width of the actuator imposes a wavelength to the separating boundary layer and the signature of this length scale can be observed downstream of the reattachment point. The role of the ZNMF actuation in modifying the energy loss is discussed. While actuators were seen to significantly reduce the reverse flow region, the vertical displacements of the mean flow streamline was still significant. As a result, present findings may suggest that reduction of separation might not necessarily lead to performance improvements for the flow device under consideration. In diffuser-type applications, for instance, the remaining large streamline displacement would continue to create flow blockage and diminish pressure recovery. For lift-generating devices, the streamline displacement forms a thicker flow envelope downstream of the leading edge, which might reduce the suction pressure peak that is typically obtained near the leading-edge. Therefore, practitioners must take the flow displacement into consideration when evaluating the benefits of actuators, and not only examining the size of the reverse-flow region.

V. Acknowledgement

The authors acknowledge the support from AFOSR Grant FA9550-17-1-0084, monitored by Dr. Douglas Smith. The simulations were performed at the Maryland Advanced Research Computing Centre (MARCC) and Stampede 2 (Texas Advanced Computing Center, TACC). The authors acknowledge discussions with Professor L. N. Cattafesta.

References

[1] Tian, Y. and Cattafesta L. N., " Adaptive control of separated flow", 44th AIAA Aerospace sciences meeting and exhibit, Reno, Nevada, 2006, pp. 1401.

[2] Buchmann, N. A., Atkinson, N. A. and Soria, J., "Influence of ZNMF jet flow control on the spatio-temporal flowstructure over a NACA-0015 airfoil". Exp. Fluids 54, 2013, pp. 1485.

[3] Seifert, A., Bachar, T., Koss, D., Shepshelovich, M. and Wygnanski, I., "Oscillatory blowing: a tool to delay boundary layer separation". AIAA J. 31, 2013, pp: 2052–2060.

[4] Seifert, A., Eliahu, S., and Greenblatt, D., "Use of piezoelectric actuators for airfoil separation control". AIAA J. 36, 1998, pp: 1535–1537.

[5] Glezer, A. and Amitay, M., "Synthetic jets". Annu. Rev. Fluid Mech. 34, 2002, pp: 503–532.

[6] Glezer, A., Amitay, M. and Honohan, A. M., "Aspects of Low- and High-Frequency Actuation for Aerodynamic Flow Control", AIAA J, 43(7), 2005, pp. 1501–1511.

[7] Seifert, A. and Pack, L. 2000. "Separation control at flight Reynolds numbers – lessons learned and future directions". Fluids 2000 Conference and Exhibit, Denver, CO, U.S.A.

[8] Yarusevych, S., Kawall, J. G., Sullivan, P. E., “Airfoil Performance at Low Reynolds Numbers in the Presence of Periodic Disturbances", Journal of Fluids Engineering 128(3), 2006, pp: 587–595.

[9] Postl, D., Balzer, W., Fasel, H. F. “Control of laminar separation using pulsed vortex generator jets: direct numerical simulations". J. Fluid Mech, 676, 2011, pp: 81–109.

[10] Yarusevych, S., Kotsonis, M., “Steady and Transient Response of a Laminar Separation Bubble to Controlled Disturbances", J. Fluid Mech, 813, 2017, pp: 955–990.

[11] Marxen, O., Kotapati, R., Mittal, R., Zaki, T., “Stability analysis of separated flows subject to control by zero-net-mass-flux jet", Phys. Fluids, 27, 2015, pp: 024107.

[12] Mittal, R., Dong, H., Bozkurttas, M., Najjar, F., Vargas, A. and von Loebbecke, A., “A versatile sharp interface immersed boundary method for incompressible flows with complex boundaries", J. Comp. Phys., 227(10), 2008, pp. 4825–4852.

[13] Mohammed-Taifour, A. and Weiss, J., “Unsteadiness in a large turbulent separation bubble", J. Fluid Mech., 799, 2016, pp: 383–412.

[14] Na, Y. and Moin, P., “Direct numerical simulation of a separated turbulent boundary layer". J. Fluid Mech., 370, 1998, pp: 175–201.

[15] Perry, A. E. and Fairlie, A. E., “A study of turbulent boundary-layer separation and reattachment", J. Fluid Mech., 69(4), 1975, pp: 657–672.

[16] Wu, W. and Piomelli, U., “Effects of surface roughness on a separating turbulent boundary layer", J. Fluid Mech., 841, 2018, pp: 552–580.

[17] Seo, J. H., Cadieux, F., Mittal, R., Deem, E. and Cattafesta, L., “Effect of synthetic jet modulation schemes on the reduction of a laminar separation bubble", Phys. Rev. Fluids, 3, 2018, pp: 033901.

[18] Meyers, J. and Meneveau, C., “Flow visualization using momentum and energy transport tubes and applications to turbulent flow in wind farms", , J. Fluid Mech., 715, 2013, pp: 335–358.

[19] Morega, A. M. and Bejan, A., “Heatline visualization of forced convection laminar boundary layers", Int. J. Heat & Mass Transfer, 36(16), 1993, pp: 3957–3966.